The distributions of slip rate and ductile deformation in a strike-slip shear zone

Frédérique Rolandone and Claude Jaupart

Institut de Physique du Globe de Paris, 4, *Place Jussieu,* 75252 *Paris, France. E-mail: rolandon@ipgp.jussieu.fr*

SUMMARY

A simple mechanical model and dimensional analysis are used to derive a scaling law for the partitioning between slip rate on a strike-slip fault and distributed deformation in the far-field. The depth of the fault, the distributions of stress, strain rate and slip rate are solved for a given far-field force or displacement in a 2-D medium with a linear temperature-dependent viscous rheology. At the shear zone axis, a mixed boundary condition is used to account for the presence of both an active fault and a ductile zone below. Over the vertical extent of the fault, the boundary condition is one of a fixed shear stress distribution dictated by a friction law. In the ductile zone below, the boundary condition is one of zero velocity. A deep fault or large vertical rheological variations are required to localize deformation on the fault with small amounts of regionally distributed deformation. In this model without thermal or strain softening, strain localization occurs naturally beneath the fault. For large rheological variations, the slip rate remains approximately constant over half the fault vertical extent and progressively decreases to zero below. Thus, there is a thick transition zone between block motion at the surface and distributed ductile deformation at depth. The near-surface deformation field depends weakly on stress and strain in the lower ductile region and the key controlling parameter is the vertical rheological variation over the depth of the fault. A scaling law relates the far-field strain rate to the slip rate and depth of the fault independently of frictional strength. For typical parameter values, the far-field strain rate is found to be $10^{-15}\,\text{s}^{-1}$ or less, showing that strike-slip faults separate blocks that can be considered rigid for all practical purposes. For the large vertical rheological variations of relevance to geological examples, shear heating is mostly a result of friction on the fault plane and is maximum at a small distance above the base of the fault.

Key words: fault models, shear heating, stress distribution, strike-slip.

1 INTRODUCTION

In active geological regions, deformation occurs in both brittle and ductile regimes. In many studies, it is assumed that lithosphere behaviour depends primarily on depth, such that the brittle–ductile transition is determined from regional estimates for the distributions of temperature and strain rate (Goetze & Evans 1979; Brace & Kohlstedt 1980). In the vicinity of a large fault, however, this assumption may be misleading because of strain localization and shear heating. In active regions, this has made comparisons between model predictions and measured displacement fields difficult. This is true for strike-slip shear zones, which account for a large fraction of tectonic deformation in many regions and are associated with devastating earthquakes. A thorough understanding of their deep structure and deformation characteristics is required to link their behaviour to far-field driving stresses and displacements. With few exceptions, strike-slip shear zones have been studied using simplified representations of the coupling between brittle and ductile layers. A velocity discontinuity is usually imposed at the base of the fault, with the slip rate kept at a constant value over the fault plane and dropping to zero just below it. This idealized representation has been used in hazard assessment, such that stress changes following earthquakes are calculated in an elastic plate of constant thickness overlying viscous material (e.g. King *et al.* 1988). It has also been used to discuss whether motions in the ductile lower crust drive, or are driven by, deformation in the shallow faulted crust (e.g. Savage 1990; Thatcher & England 1998; Bourne *et al.* 1998; Savage *et al.* 1999). Such a simple representation may not be correct and one should determine the vertical distribution of slip rate and the size of the transition zone where deformation has both slip and ductile components.

The behaviour of a fault zone depends on several variables, including frictional strength, rheology of crustal rocks, thermal structure and far-field stresses. In practice, therefore, it is desirable to develop some understanding of the role of each variable and how each one affects the slip and ductile components of deformation in both the horizontal and vertical directions. Both types of deformation generate shear heating and it is important to specify their respective contributions when evaluating the implied thermal perturbations (e.g. Lachenbruch & Sass 1980, 1992; Scholz 1980; Turcotte *et al.* 1980; Ricard *et al.* 1983; Thatcher & England 1998; Leloup *et al.* 1999). For example, one might argue that frictional heat caused by slip on the fault surface may be evacuated locally through fluid circulation, as fault gouges may be permeable (Sleep & Blanpied 1992; Scholz 2000; Townend & Zoback 2000). Shear heating is likely to reach a maximum near the base of the fault, where shear stresses are largest and where deformation is likely to have both slip and ductile components.

In this paper, we develop a mechanical model of a shear zone in a ductile medium driven by far-field stresses or displacements. We determine the relationships between the depth of the fault, the vertical distribution of slip rate and the ductile deformation field, as functions of far-field boundary conditions, thermal structure and rheological parameters. For clarity, the study is restricted to steady-state conditions, but is intended to serve as the starting point for a fully time-dependent description of a shear zone. Our approach has several characteristics in common with recent studies. In Roy & Royden (2000), brittle faulting is represented by elastic dislocations in a linear visco-elastic medium with depth-dependent viscosity. The slip rate is kept at a uniform value over fault surfaces and the depth and spacing of faults are solved for. Chery *et al.* (2001) have studied the behaviour of a fault zone in a temperature-dependent linear ductile medium subject to a range of far-field conditions and rheological variations. They specify the width of the shear zone and do not study shear heating. In this paper, we consider a large parameter range and use dimensional analysis to shed light on the key control variables. This also allows extrapolations to other cases. We evaluate the various components of shear heating and demonstrate how they change as a function of the control variables.

2 MODEL FORMULATION

2.1 Deformation mechanisms in the continental crust

Knowledge on the mechanical behaviour of the upper crust has improved considerably over the previous two decades thanks to material science studies and field observations (Sibson 1986; Kohlstedt *et al.* 1995) (Fig. 1). At shallow depths, heavily fractured and jointed rocks behave as unconsolidated granular material. Thus, deformation proceeds by frictional sliding on randomly oriented fractures, leading to a linear increase of deviatoric stress with depth known as Byerlee's rule (Byerlee 1978; Brace & Kohlstedt 1980). With increasing depth, the frictional strength increases and the macroscopic behaviour depends on whether rocks are intact or pervasively faulted. Stresses become sufficiently large for the activation of mechanisms driving regionally distributed deformation. Depending on temperature, stress and the presence or absence of fluids, such mechanisms may include non-localized cataclastic ductile flow, semi-brittle flow involving both plastic and brittle processes,
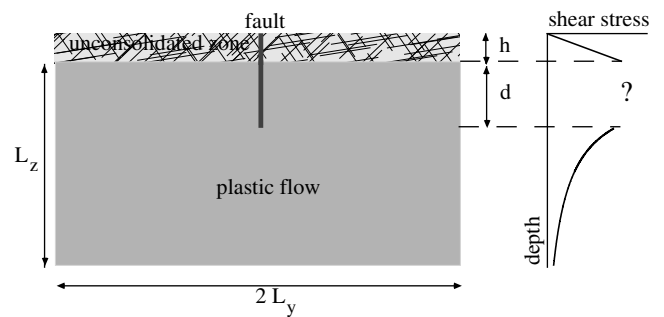

Figure 1. Schematic illustration of the mechanical behaviour of the continental lithosphere. A thin uppermost layer of about 3 km thickness is made of heavily jointed rocks and behaves as unconsolidated granular material (Scholz 1998). Below this layer, a major fault extends over thickness *d* and material deforms in a ductile regime. Brittle and ductile deformation mechanisms depend on the local values of stress and strain rate and cannot be imposed *a priori*. On the right is shown a schematic representation of the vertical stress profile. In the thin unconsolidated layer, stresses increase linearly with depth according to Byerlee's rule. In the lower crust, plastic deformation is such that stresses decrease with increasing depth. In the intermediate region, deformation gets localized in the vicinity of the fault, implying lateral variations of stress and strain rate.

power-law breakdown creep or grain boundary diffusion creep (Kohlstedt *et al.* 1995). With such mechanisms, strain rates in geological conditions are necessarily small, but the question of exactly how small they can be motivates the present analysis. At sufficiently large depths, temperatures are large enough for fully plastic flow processes to dominate. Specifying constitutive equations for the various regimes represents a formidable challenge for the heterogeneous continental crust made of water-bearing rocks with large variations of mineralogy and texture (Kohlstedt *et al.* 1995).

In the simplest model, the transition from brittle to plastic flow is such that the frictional strength exceeds the plastic flow stress. This will be referred to as the brittle–ductile transition in order to follow common usage, although it is a rather gross approximation. The depth of this transition decreases with decreasing strain rate, and may vary between depths of 6 and 25 km depending on rock type (Kohlstedt *et al.* 1995). Most calculations are made with the strain rate set at $10^{-15}\,\text{s}^{-1}$, on the grounds that smaller values are not geologically significant, i.e. lead to displacements that are not relevant for tectonic studies. In reality, this assumption glosses over one of the key goals of tectonic studies, which is to assess whether continental deformation is achieved through faults separating rigid blocks or involves a significant component of regional strain. In a region where a major fault extends through a large part of the 'brittle' crust, we are interested in how strain is partitioned between sliding on the fault and regionally distributed deformation. To solve this problem, one must determine slip rates on the fault and strain rates away from the fault in a self-consistent manner. This issue may be discussed using the San Andreas fault system as an example. There, recent high-resolution images of seismicity emphasize that earthquakes are concentrated in a few very thin shear zones down to depths that typically exceed 10 km (Schaff *et al.* 2001). Furthermore, at distances greater than about 50 km from the San Andreas fault, strain rates fall below detection levels and, in fact, below the reference value of $10^{-15}\,\text{s}^{-1}$ (Thatcher 1990). These observations suggest that, at

depth and away from a major fault, stresses do not reach the local frictional strength and raise the important question of how such values of strain rate are achieved.

Byerlee's rule specifies the stress profile for brittle crust, but provides no constitutive equation between stress and strain rate. Thus, for a given far-field driving force, displacements in such material cannot be predicted by a mechanical model. This explains why most studies of continental deformation rely on kinematic boundary conditions and on assumptions for the coupling between brittle and ductile layers (e.g. Thatcher & England 1998). One important issue is whether stresses are only depth-dependent and remain equal to the frictional strength along the horizontal. There is little doubt that this is true at very shallow depths in what may be called the 'unconsolidated' region. This is a region of 'frictional stability', such that earthquakes cannot be generated, which extends over 3 to 4 km (Mori & Abercrombie 1997; Scholz 1998). In such weak material, there is not much resistance to slip. Thus, there is no meaningful limitation on strain rates, and one may assume that displacements follow passively those of the substrate. Below this shallow region, the frictional strength becomes large and the vertical extent over which it may be overcome depends on two factors. One is the magnitude of the driving tectonic force, and the other is how this force is partitioned between brittle and ductile regions. This difficulty led Thatcher & England (1998) to define two end-member possibilities. In one of them, the ductile layer is strongest and drives deformation in the passive upper crust. This extends the unconsolidated region to the whole seismogenic upper crust. In this case, the top of the ductile layer behaves as a traction-free surface and deformation is driven by basal shear. In the other end-member, the brittle region is the strongest part of the crust and drives deformation in the ductile lower crust. A fault is separated by rigid blocks and a stepwise change of velocity deduced from field studies is introduced as a boundary condition at the top of the ductile layer. One problem with these models is that, given that rather large horizontal stress variations are predicted in the ductile medium, there is no reason to believe that the brittle–ductile transition lies at a fixed depth.

2.2 Governing equations

In the present model, the uppermost unconsolidated crustal layer of thickness h is not taken into account. We assume that this layer is 'passive', such that displacements follow those of the substrate. Below this layer, distributed deformation occurs away from one major fault (Fig. 1). A large fraction of the far-field tectonic displacement is taken up by sliding on the fault and strain rates are small away from the fault. For such low strain rate deformation, we use a single temperature-dependent flow law. There are large uncertainties on crustal rheology and frictional strength, and hence our aim is to establish scaling laws that allow compact information independent of specific, and probably unreliable, choices of constitutive equations and parameter values.

We do not consider the short-term earthquake cycle and focus on the long-term behaviour, i.e. the secular slip rate on the fault owing to the tectonic loading of the bounding blocks. As a first step, the study is restricted to steady-state thermal conditions with a temperature field that depends on depth only. In 2-D, motion occurs only in the horizontal direction

parallel to the vertical shear zone, such that the velocity vector $\mathbf{v} = (v_x, 0, 0)$ and there are no along-strike variations (along the x axis) (Fig. 2). Conservation of momentum in the x-direction is written as follows:

$$\frac{\partial \sigma_{yx}}{\partial y} + \frac{\partial \sigma_{zx}}{\partial z} = 0, \tag{1}$$

where σ_{yx} and σ_{zx} are the components of the stress tensor.

Following Yuen *et al.* (1978), Thatcher & England (1998) and Chery *et al.* (2001), we use a temperature-dependent linear isotropic viscous rheology for crustal and mantle rocks. One reason for this approximation is that, with a suitable choice of parameters, such a simplified rheology allows good agreement with vertical stress profiles derived from laboratory studies (Chery *et al.* 2001). The relationship between deviatoric stress and strain rate is therefore

$$\sigma_{ij} = 2\mu\dot{\varepsilon}_{ij}, \tag{2}$$

where μ is the temperature-dependent viscosity and $\dot{\varepsilon}_{ij}$ the strain rate. The momentum equation is rewritten as follows:

$$\frac{\partial}{\partial y}\left(\mu \frac{\partial v_x}{\partial y}\right) + \frac{\partial}{\partial z}\left(\mu \frac{\partial v_x}{\partial z}\right) = 0. \tag{3}$$

This study is intended as a starting point for time-dependent calculations where the temperature field varies in both the horizontal and vertical directions owing to shear heating. Thus, viscosity must be considered to be temperature-dependent:

$$\mu = \frac{T}{2B} \exp\left(\frac{E}{RT}\right), \tag{4}$$

where T is the temperature, B is a material constant, E is the activation energy and R is the universal gas constant. In the following, the temperature varies only with depth ($T = T_0 + \beta z$), and hence so does viscosity. Later on, we shall define a depth-scale for vertical viscosity variations as a function of both E and β.

In all calculations but one, the whole domain is characterized by a single flow law. In reality, crustal and mantle rocks have different rheologies but we shall show that the fault behaviour is not sensitive to the rheology of deep material. We have made calculations for a range of activation energies, implying different rheological stratifications for the ductile medium. For dislocation creep in continental crustal rocks, constitutive relationships between strain rate and stress are power laws with values of the activation energy and exponent varying between about 100 and 300 kJ mol^{-1} and between about 2 and 3, respectively (Carter & Tsenn 1987; Kirby & Kronenberg 1987; Kohlstedt
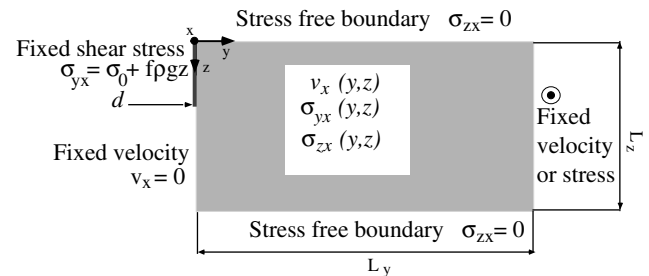

Figure 2. Geometry and boundary conditions of the mechanical model. Boundary conditions are in bold letters, and the variables to be solved for are in italics.

et al. 1995). For geological strain rates, depending on temperature, the same stress levels are achieved by a linear rheology with values of the activation energy between about 70 and 110 kJ mol^{-1} (Chery *et al.* 2001).

2.3   Boundary conditions

The behaviour of the shear zone at the axis is determined by the vertical shear stress profile, and the slip rate on the fault is not prescribed because this is the variable we seek to determine. If stresses at the axis overcome the frictional resistance, the fault is activated and some fraction of the total displacement is taken up by sliding. On the contrary, if stresses are lower than the frictional strength, there is no slip on the fault. The base of the fault does not correspond to a fixed material discontinuity, but lies at a depth that is dictated by the local stress field. Below the fault, deformation occurs in the ductile regime and there is no slip.

Given the large uncertainties on the true values of shear stress on faults (e.g. Scholz 2000; Zoback 2000), we consider two different constitutive equations for the fault. We use a simple Amonton friction law with constant friction coefficient and an alternative model in which the threshold shear stress for sliding is constant, corresponding to zero friction coefficient. Assuming that the principal contribution to the normal stress is lithostatic pressure, the friction law states that the shear stress on the active fault increases linearly with total depth z^*:

$$\sigma_{yx} = \sigma_c + f\rho g z^*, \tag{5}$$

where σ_c denotes cohesion and f is a constant friction coefficient. The top of the computational domain (at $z=0$) lies at depth h below an unconsolidated layer. Thickness h needs not be specified and only affects stress levels on the fault. In our coordinate system, the frictional law is rewritten as

$$\sigma_{yx} = \sigma_0 + f\rho g z, \tag{6}$$

where the 'effective' cohesion coefficient σ_0 includes the contribution of friction associated with the weight of the overburden:

$$\sigma_0 = \sigma_c + f\rho g h. \tag{7}$$

In summary, for the mechanical model, the shear zone axis at the left-hand edge of the domain is defined by a mixed boundary condition, a shear stress profile dictated by the friction law over the fault and a fixed velocity ($v_x=0$) below. Far from the fault plane, the medium has a block-like behaviour with no vertical gradients of strain rate and displacement. Strike-slip motion arises from a constant driving force that, in the steady state, corresponds to both a fixed displacement rate and a fixed stress distribution. At the top of the domain, unconsolidated material offers no resistance to slip, which corresponds to stress-free boundary conditions. The base of the computational domain at high temperatures is also taken to be traction free. Fig. 2 illustrates schematically the mechanical model and its boundary conditions.

2.4   Method and aims

In order to account for large variations of physical properties and small-scale stress gradients, we have used a finite-element method. For given far-field conditions, the depth d of the fault,

the vertical distribution of the slip rate on the fault and the deformation rates elsewhere are solved for. Geological systems involve large vertical rheological variations and we have investigated cases where the viscosity varies by as much as 3×10^{13} in order to generate the large range of conditions needed to establish scaling laws. Calculations were carried out over a non-uniform grid with 900×900 elements, such that the smallest elements in the vicinity of the fault plane are 31 m wide. For typical parameter values (Table 1), results were obtained in a half-space with 95 km depth and 200 km wide—broad enough that it does not influence the local behaviour of the shear zone. These physical dimensions may be thought of as being representative of the continental lithosphere in an active region, but, as will be made clear later, do not influence the results in any important way.

The accuracy of the solutions was ascertained in two ways. Calculations on a finer mesh-size do not differ significantly. A second test is provided by verifying that the total applied force is conserved. With our boundary conditions (Fig. 2), eq. (1) imposes that

$$\int_0^{L_z} \sigma_{yx}\, dz = F, \tag{8}$$

where L_z is the depth of the domain. F is the total shear force and does not depend on y, the distance from the shear zone. For our numerical results, condition (8) is satisfied at all distances (y) to better than ± 2 per cent.

3   FAULT DEPTH AND DEFORMATION

Results are given first for a specific set of parameter values that are not meant to be fully realistic (Table 1). Variables will be shown in dimensionless form and the scaling analysis will allow a general understanding independent of the specific values chosen. At the top of the model, the viscosity is fixed arbitrarily at a value $\mu_0 = 10^{26}$ Pa s, close to the values given by Thatcher & England (1998). Other parameters are the friction coefficient $f=0.6$ (Byerlee 1978), density $\rho = 3 \times 10^3$ kg m^{-3} and 'effective' cohesion $\sigma_0 = 90$ MPa, which corresponds to the frictional strength at a depth of 5 km. We also take a fixed geotherm with gradient $\beta = 0.01$ K m^{-1} and $T_0 = 323$ K. Stresses are normalized using the maximum stress on the fault:

$$\sigma_d = \sigma_o + f\rho g d. \tag{9}$$

Slip and displacement rates are normalized using the far-field velocity at the right-hand boundary:

$$U_f = v_x(L_y, z). \tag{10}$$

Table 1. Parameter values for most calculations.

Viscosity at the upper boundary	μ_0	10^{26} Pa s
Average density	ρ	3×10^3 kg m^{-3}
Cohesion	σ_0	90 MPa
Friction coefficient	f	0.6
Geothermal gradient	β	0.01 K m^{-1}
Upper boundary temperature	T_0	323 K
Width of computational domain	L_y	200 km
Thickness of computational domain	L_z	95 km

With the linear rheology, these normalization procedures lead to dimensionless variables that are independent of the viscosity scale μ_0.

In each calculation, the far-field driving force F is imposed. In the steady state, this is equivalent to specifying the far-field displacement at some value that depends on the rheology and thermal structure. Five different cases with different parameter values will be described in detail (Table 2). We shall also present two sets of calculations in which a single parameter is changed. In the first set, the driving force F varies, implying different fault depths d. In the second set, we investigate how changes of rheological stratification affect the fault behaviour and stresses. Changes of rheological structure are generated by changes of activation energy, but each case is identified by the total viscosity variation in the domain, μ_0/μ_b, where μ_b is the basal viscosity at $z = L_z$.

3.1 The distributions of velocity, slip rate and shear stress

In model 1 (Table 2), we impose a relatively small far-field force F and take an activation energy of 95 kJ mol^{-1}, implying a vertical viscosity variation of *ca.* 11 orders of magnitude (Fig. 3). In this case, a shallow fault with $d = 5$ km deep is activated. Such a shallow fault barely modifies the velocity field in the lithosphere (Fig. 4).

The far-field velocity at the right-hand edge of the domain, at $y = L_y$, is denoted by U_1. At the top of the domain, sliding on the fault accounts for only 15 per cent of U_1. The deformation is distributed quite evenly over the whole width of the domain and strain rates are almost uniform along the vertical. On the fault surface, the slip rate remains approximately constant over a small vertical distance and decreases progressively towards zero at $z = 5$ km (Fig. 5). There is no well-defined surface over which the slip rate is uniform, and there is instead a large adjustment zone where the deformation proceeds by both slip and ductile flow.

Shear stress follows the friction law down to the calculated fault depth d, by definition, and decreases sharply below in the region where all deformation occurs in the ductile regime (Fig. 6). The stress field changes dramatically as one moves away from the shear zone (Fig. 7).

Model 2 has the same rheological structure as model 1 and a larger driving force, which leads to a larger far-field velocity U_2 ($U_2 = 32U_1$). Consequently, a deeper fault, $d = 12$ km, is
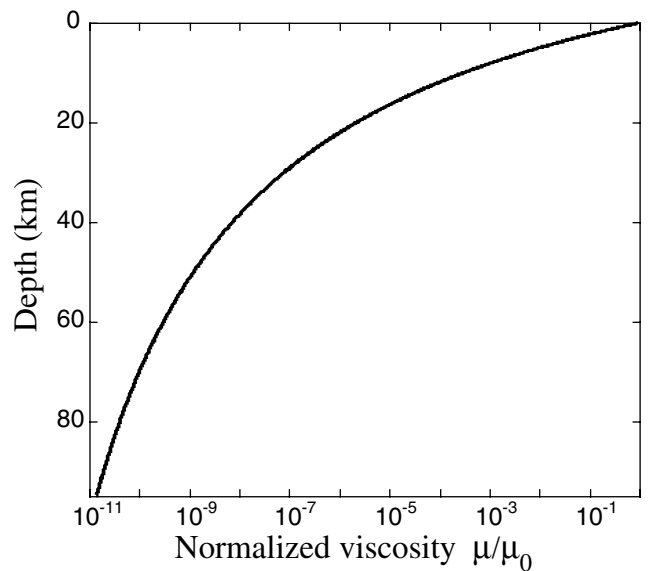

Figure 3. Vertical distribution of viscosity normalized to the largest viscosity at the top of the model, μ_0, for models with fixed rheological stratification, including models 1 and 2 (Table 2).

activated, and this modifies the velocity pattern markedly (Fig. 8). Near the surface, the fault now accounts for most of the motion: at the upper boundary, the slip rate is 92 per cent of the far-field velocity. Thus, the upper part of the domain
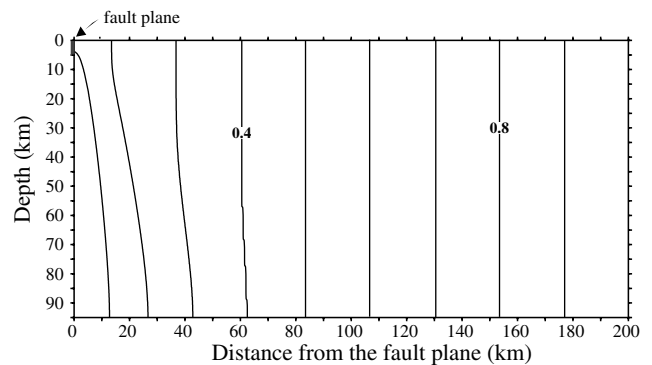

Figure 4. Velocity field for model 1 (Table 2). Velocity values have been normalized by the far-field velocity at the right-hand side of the domain, $U_f = v_x(L_y, z)$. Contours are shown for 0.1 increments. A shallow fault 5 km deep is activated, which only affects the ductile deformation pattern in a small region.

Table 2. Parameter values for five cases.

Model	Cohesion σ_o (MPa)	Friction coefficient f	Activation energy E (kJ mol^{-1})	Total vertical viscosity variation μ_0/μ_b	Driving force F (N m^{-1})	Fault depth d (km)	Normalized slip rate U_s/U_f
1	90	0.6	95	7.33×10^{10}	9.0×10^{11}	5	0.15
2	90	0.6	95	7.33×10^{10}	2.8×10^{12}	12	0.92
3	90	0.6	105	1.18×10^{12}	2.2×10^{12}	10	0.87
4 †	90	0.6	105	2.90×10^{7}	2.2×10^{12}	10	0.87
5 ‡	180	0	105	1.18×10^{12}	2.2×10^{12}	10	0.87

†: Model with truncated viscosity profile (see text and Fig. 12).

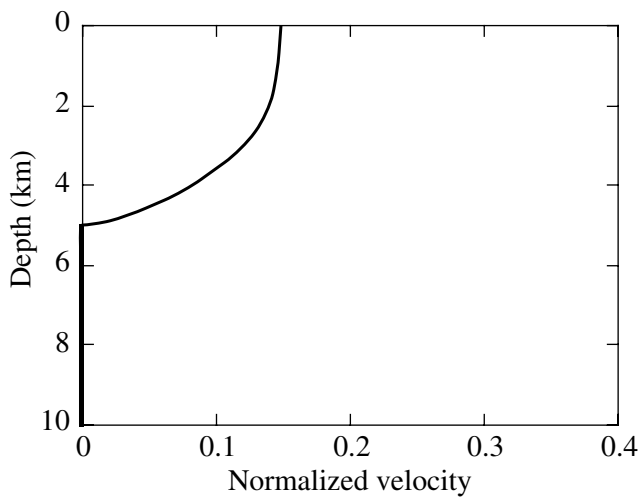‡: Model with constant shear stress on the fault (see text).

Figure 5. Vertical profile of slip rate on the fault plane for model 1, normalized to the far-field value at the right-hand side boundary, U_f.

has a quasi-rigid behaviour with negligible distributed ductile deformation. The deformation is confined to the vicinity of the fault and strain rates are very small away from the fault. At depth, deformation is also concentrated in the vicinity of the fault axis, even in the ductile region below the fault.

For a given rheological stratification, a higher driving force or far-field velocity activates a deeper fault. If we focus on the fault itself, however, and compare the vertical profiles of the slip rate on the fault for models 1 and 2, we can see that the differences are small (Fig. 9). For the deeper fault, block motion is achieved over a slightly thicker region at the top and, correspondingly, the transitional region with both slip and ductile components is smaller. The stress fields for models 1 and 2 look similar when allowance is made for the different fault depths. However, the deformation fields differ markedly, because of the different slip rate magnitudes. At the regional scale, the shallower fault does not modify the velocity field and does not take up a significant fraction of the deformation. With a larger
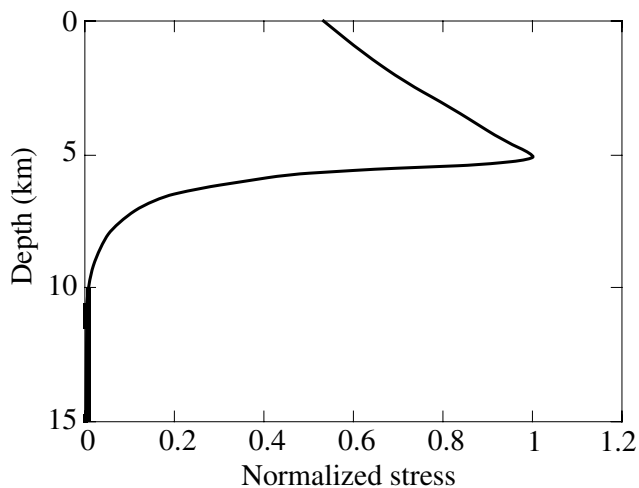

Figure 6. Vertical distribution of shear stress $\sigma_{yx}(0, z)$ at the shear zone axis for model 1. Stresses correspond to the friction law down to the base of the fault at depth $d = 5$ km.
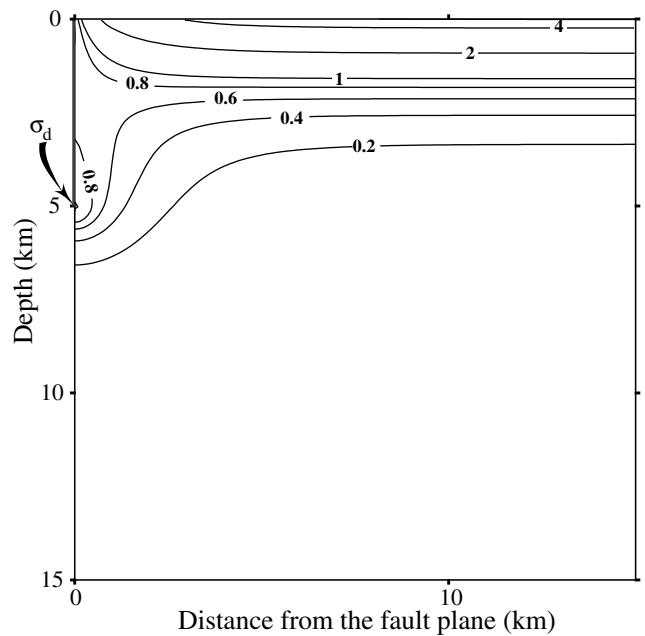

Figure 7. Shear stress field σ_{yx} for model 1. Shear stress values have been normalized by the maximum stress on the active fault, $\sigma_d = \sigma_0 + f\rho g d$.

driving force, the fault roots deeper and, near the surface, deformation is mainly achieved by slip on the fault. At depth, strain is localized in a relatively narrow shear zone beneath the fault. This is achieved without elevated temperatures near the fault.

3.2 Fixed rheological stratification and variable fault depth

In a first set of calculations (Table 3), we have kept the same rheological structure (Fig. 3) and have considered a range of values for the driving force F. Increasing the driving force acts to increase shear stress values at the axis, and hence to deepen the fault. As the fault depth increases, sliding on the fault accounts for an increasing fraction of the total deformation. A measure of this is provided by the ratio of the slip rate to the far-field velocity, U_s/U_f (Fig. 10). For the deepest fault ($d = 15$ km), this ratio reaches a value of 0.98, i.e. distributed deformation only accounts for 2 per cent of the far-field displacement.

Table 3. Parameter values for calculations in which the driving force F is the only variable parameter. The activation energy for ductile flow is kept constant, corresponding to a vertical rheological variation, μ_0/μ_b, of 7.3×10^{10}. All other parameters (Table 1) are kept constant.

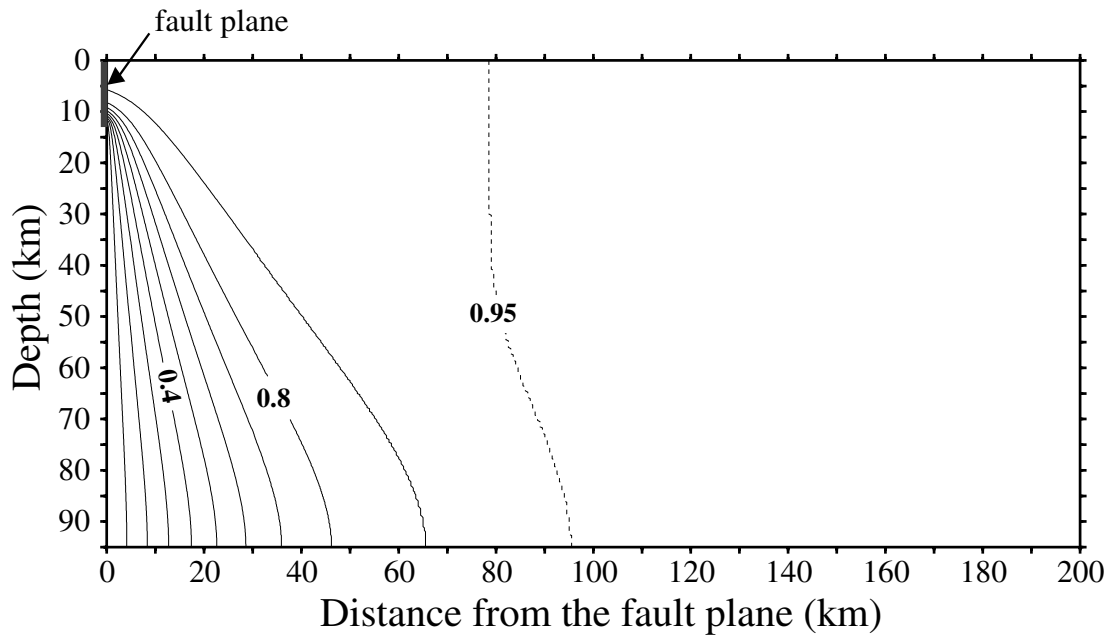| Driving force F (N m^{-1})	Fault depth d (km)	Normalized slip rate U_s/U_f
9.0×10^{11}	5	0.15
1.4×10^{12}	7	0.46
2.0×10^{12}	10	0.80
2.8×10^{12}	12	0.92
3.7×10^{12}	15	0.98

Figure 8. Velocity field for model 2. Velocity values have been normalized by the far-field velocity U_f. Solid contours are shown at steps of 0.1. The vertical rheological variation is the same as in model 1, but a higher driving force is applied. With respect to model 1 in Fig. 4, far-field strain rates are much smaller, showing that rigid behaviour is achieved. Horizontal velocity gradients are large in a deep ductile shear zone below the fault, showing that strain localization occurs at depth without local thermal softening.

3.3 Variable rheological stratification and fixed fault depth

In this second set of calculations, we have kept the fault depth at a constant value $d = 10$ km and have varied the activation energy for ductile flow, implying changes of vertical rheological variation (Table 4). For these calculations, the driving force F is almost constant. As the vertical viscosity variation is increased, the upper part of the domain becomes increasingly stiffer than the lower part, implying that deformation is increasingly taken up by sliding on the fault. Thus, the ratio of the slip rate to the far-field velocity, U_s/U_f, increases (Fig. 11).

Table 4. Parameter values for calculations with fixed fault depth $d = 10$ km and variable activation energy for ductile flow. All other parameters (Table 1) are kept constant.

Activation energy E (kJ mol^{-1})	Vertical viscosity variation μ_0/μ_b	Normalized slip rate U_s/U_f
75	2.84×10^8	0.38
82	1.99×10^9	0.59
90	1.83×10^{10}	0.77
95	7.30×10^{10}	0.80
105	1.18×10^{12}	0.87
110	4.73×10^{12}	0.90
117	3.32×10^{13}	0.93

3.4 Local behaviour in the vicinity of the fault

We have seen that the deformation characteristics depend on the vertical rheological variation between the top and the bottom. However, we have also seen that the largest stresses are limited to the vicinity of the fault. This suggests that the lower part of the domain, where viscosity is lowest, does not affect the upper part. To verify this, we have considered two models with different viscosity structures in the lower part of the domain, numbered 3 and 4 (Table 2). Both have faults extending to the same depth $d = 10$ km. Model 3 has a large vertical rheological variation of 12 orders of magnitude. In model 4, the vertical viscosity profile of model 3 is truncated at 27 km depth, which generates a more viscous substratum (Fig. 12).

The velocity fields for models 3 and 4 are almost identical in the upper part of the domain, both near the fault and at a large horizontal distance from it (Figs 13 and 14), but are markedly different from one another in the lower part of the domain. This shows that the low-viscosity region at the base of the domain
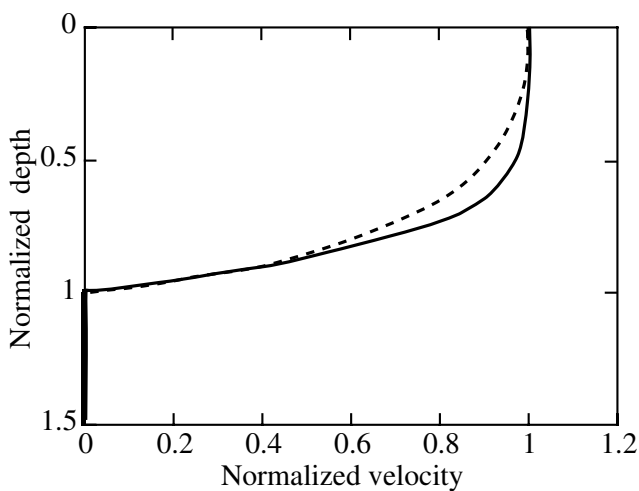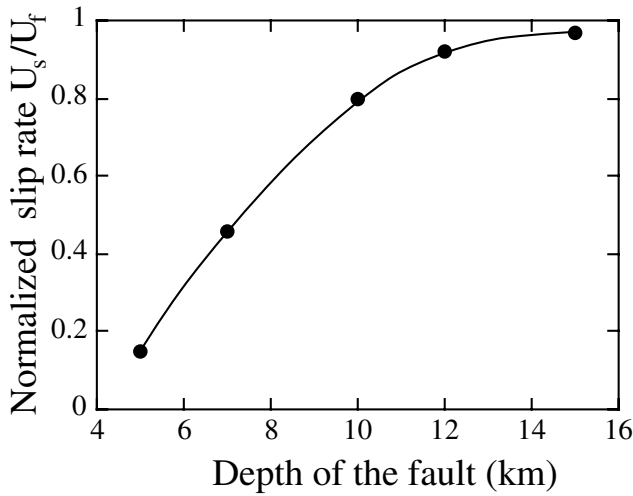

Figure 9. Vertical profiles of slip rate for model 1 (dashed line) and model 2 (plain line). To facilitate the comparison, depth and slip rate have been normalized by fault depth d and by the maximum slip rate at the top of the fault, $U_s|_{z=0}$, respectively.

Figure 10. Normalized slip rate U_s/U_f as a function of fault depth d for models in which the activation energy is kept constant. The total vertical viscosity variation across the domain, μ_0/μ_b, is 7.3×10^{10} for all cases.

has little influence on fault behaviour and on how deformation becomes localized at shallow levels. The deep viscosity structure only influences the width of the basal shear zone. One should not conclude from this that the upper and lower regions are mechanically decoupled, because the regional stress fields are similar.

We have also considered a different friction law in order to evaluate its impact on the results. Model 5 has the same characteristics as model 3 (Table 2), save for the stress distribution on the fault. This was set to a constant value equal to the average shear stress in model 3 (equal to $\sigma_0 + \frac{1}{2} f\rho g d$). We found that the velocity pattern is not modified in any significant manner and that the slip rate on the fault takes the same value in both cases (Table 2). The only noticeable differences are in the local stress field near the fault (Figs 15 and 16). We note,
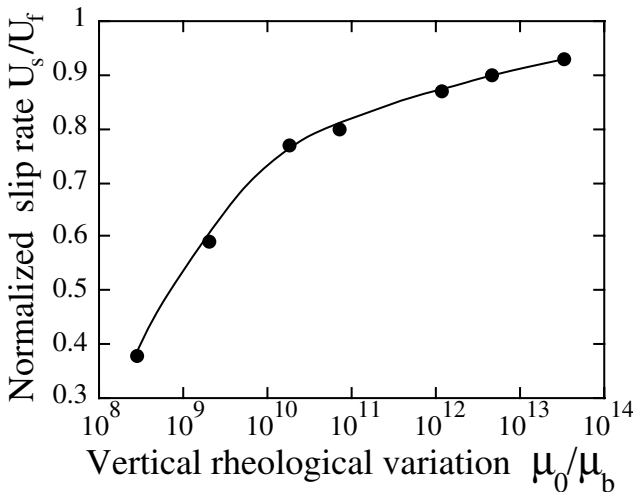

Figure 11. Normalized slip rate U_s/U_f as a function of the total vertical viscosity variation, μ_0/μ_b, for models in which the depth of the fault is kept at a constant value of $d = 10$ km. Calculations are made for different values of the activation energy for ductile flow, corresponding to different values of μ_0/μ_b.
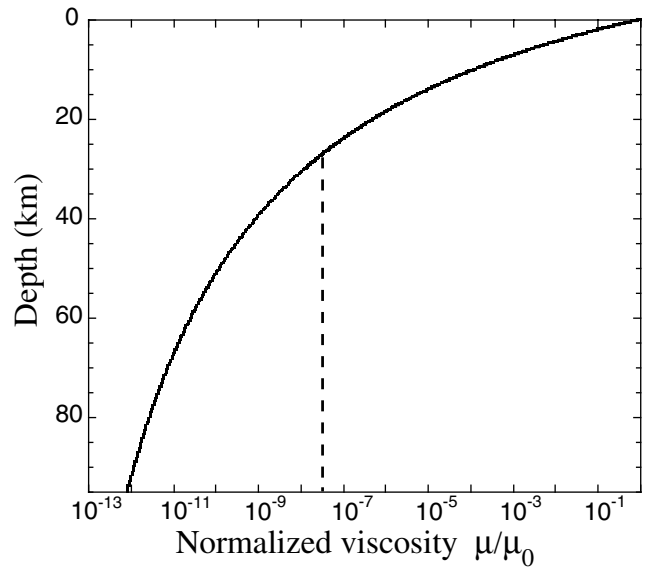

Figure 12. Viscosity profiles normalized to the largest viscosity value at the top of the model, μ_0. The plain profile corresponds to model 3 and the dashed line shows how this profile has been truncated for model 4.
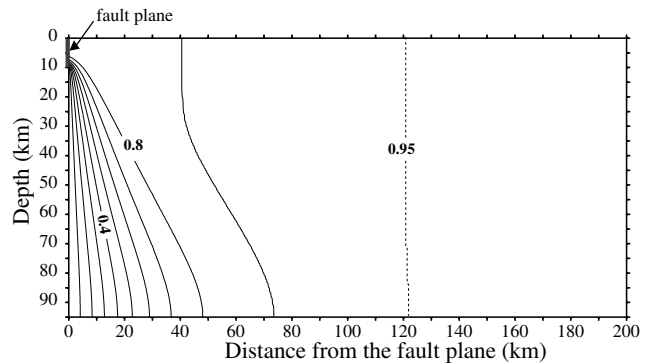

Figure 13. Velocity values normalized to the far-field velocity U_f for model 3. Solid contours are shown at steps of 0.1 as for models 1 and 2. The depth of the fault is fixed at $d = 10$ km and the vertical viscosity profile is shown in Fig. 12. As in model 2, most of the deformation is accommodated by sliding on the fault.
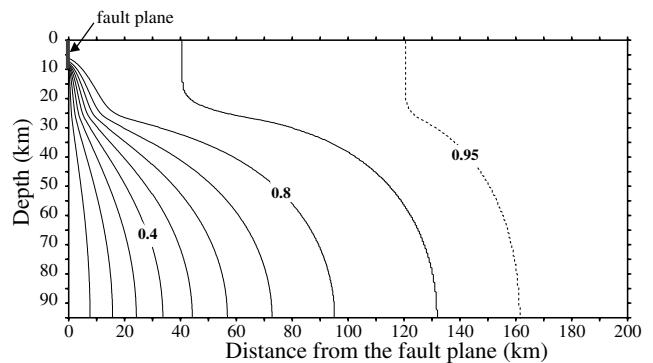

Figure 14. Velocity values normalized by the far-field velocity U_f for model 4 with the truncated viscosity profile of Fig. 12. Only the deep viscosity distribution has been changed with respect to model 3. In the upper part of the domain, above 20 km, there are no differences between the two sets of results (Fig. 13).
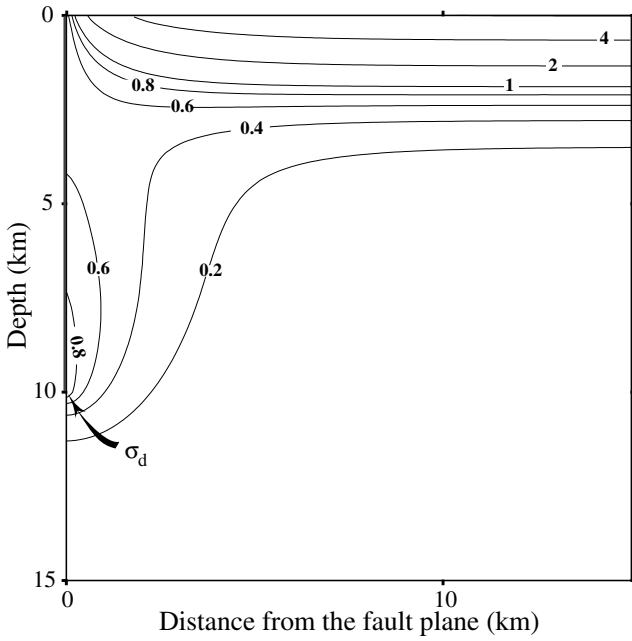
Figure 15. Shear stress field σ_{yx} for model 3. Shear stress values have been normalized by the maximum stress on the active fault, $\sigma_d = \sigma_0 + f\rho g d$.

however, that these differences disappear at a small horizontal distance (approximately equal to the fault depth d) from the fault.

4 PHYSICAL ANALYSIS

We have seen that, for a given vertical rheological variation, increasing the far-field force implies a deeper fault and stronger strain localization near the fault. For a fixed fault depth,
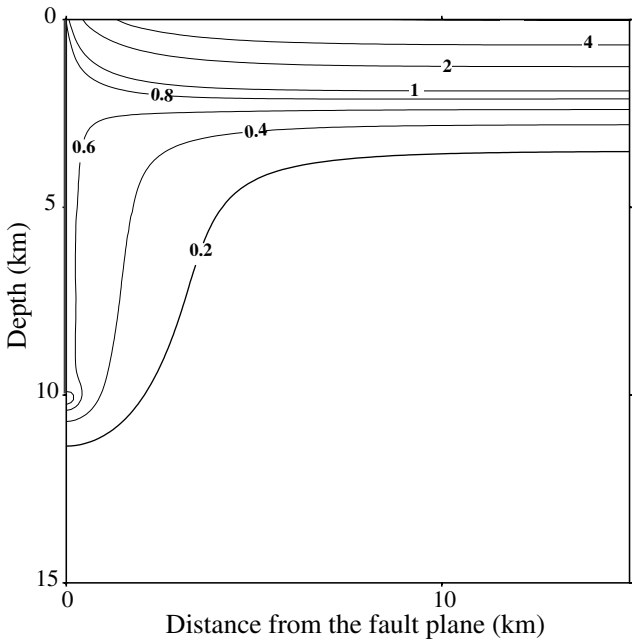

Figure 16. Shear stress field σ_{yx} for model 5. The friction law is replaced by a fixed shear stress on the fault equal to the average shear stress in model 3. Shear stress values have been normalized by the same value σ_d.

increasing the vertical rheological variation between the top and the bottom also leads to strain focusing. In fact, both series of calculations achieve the same effect: increasing the depth of the fault acts to increase the vertical rheological variation over the active fault, with the same consequence. Furthermore, we have found that the rheological structure at great depth does not affect the fault behaviour. These two results suggest that the main controlling variable is the vertical variation of rheology over the depth of the fault.

4.1 Scaling analysis

Calculations require a large number of input parameters, such as the friction coefficient, the activation energy for ductile flow and the total far-field force. Different variables are sensitive to different input parameters, and it is useful to make these various relationships explicit. In the previous sections, the importance of ductile deformation was assessed using the ratio of the slip rate to the far-field velocity, U_s/U_f. The problem with this procedure is that, for a given strain rate, however small it may be, the far-field velocity increases with the width of the computational domain. It is more appropriate to seek an intrinsic strain rate scale, which allows a measure of ductile deformation independent of domain size. The far-field strain rate G provides such a scale and, as shown by eq. (13), is a simple function of the driving force and the vertical viscosity function.

At the right-hand side of the domain, far from the fault plane, velocity does not vary with depth. Thus, one has

$$\frac{\partial v_x(L_y, z)}{\partial z} = 0, \tag{11}$$

and hence, using the momentum eq. (3):

$$\frac{\partial v_x(L_y, z)}{\partial y} = G, \tag{12}$$

where G is the far-field strain rate which does not depend on depth. The total applied shear force is

$$F = \int_0^{L_z} \sigma_{yx}(L_y, z)\, dz = G \int_0^{L_z} \mu(z)\, dz. \tag{13}$$

It is convenient to define a depth-scale for viscosity variations:

$$\delta = \frac{\int_0^{L_z} \mu(z)\, dz}{\mu_0}. \tag{14}$$

Changing variables in the viscosity integral leads to

$$\int_0^{L_z} \mu(z)\, dz = \frac{1}{2B} \frac{E^2}{aR^2} \int_{RT_0/E}^{RT_b/E} \theta \exp(1/\theta)\, d\theta, \tag{15}$$

where $T_b = T(L_z)$ is the temperature at the base of the domain. The integrand decreases rapidly and the integral is for all practical purposes independent of the upper bound. This is written as follows:

$$\int_0^{L_z} \mu(z)\, dz \approx \frac{1}{2B} \frac{E^2}{aR^2} \int_{RT_0/E}^{\infty} \theta \exp(1/\theta)\, d\theta = \frac{1}{2B} \frac{E^2}{aR^2} h_1(\theta_0), \tag{16}$$

where h_1 is a dimensionless function of dimensionless variable $\theta_0 = E/RT_0$. From this, one has

$$\delta = \frac{E}{\beta R} \frac{h_1(\theta_0)}{\theta_0 \exp(1/\theta_0)} = \frac{E}{\beta R} h_2(\theta_0),\tag{17}$$

where $E/\beta R$ has the dimensions of depth and the function h_2 is also dimensionless. δ provides a depth-scale for viscosity variations and depends on the temperature gradient and rheological parameters. Far from the fault plane, the total force is therefore given by

$$F = G\mu_0\delta.\tag{18}$$

On the left-hand side of the domain, one may write

$$F = \int_0^d \sigma_{yx}\,dz + \int_d^{L_z} \sigma_{yx}\,dz.\tag{19}$$

The second term is very small (see Fig. 6) and hence

$$F \approx \int_0^d \sigma_{yx}\,dz \approx \int_0^d (\sigma_0 + f\rho gz)\,dz = \sigma_0 d + \frac{1}{2} f\rho gd^2.\tag{20}$$

This shows how the total applied force determines the length-scale of our problem. We define a depth-scale $[d]$ such that

$$F = \sigma_0[d] + \frac{1}{2} f\rho g[d]^2.\tag{21}$$

This scale is close to the true fault depth d, as expected from eq. (20) and as shown below. One may introduce another depth-scale, d_c, such that

$$f\rho gd_c = \sigma_0.\tag{22}$$

For a large driving force or small cohesion, i.e. large values of $F/\sigma_0 d_c$, eq. (21) simplifies:

$$\text{for large } \frac{F}{\sigma_0 d_c}, \quad [d] \approx \sqrt{\frac{2F}{f\rho g}}.\tag{23}$$

This shows how the driving force imposes the vertical extent of the active fault for given friction parameters.

Using the same line of reasoning, the stress scale is given by the friction law:

$$[\sigma] = \sigma_0 + f\rho g[d] = \sqrt{\sigma_0^2 + 2f\rho gF}.\tag{24}$$

We have scales for the depth, $[d]$, as well as for the strain rate, G, and hence a velocity scale:

$$[U] = [d]G.\tag{25}$$

This velocity value corresponds to the cumulative effect of ductile deformation away from the fault, and provides a scale for plastic flow which may be compared with the maximum slip rate on the fault, U_s. The ratio between these two velocity values provides a convenient way to assess the importance of slip in the near-surface deformation field. For a large force or negligible cohesion, equations for the velocity and stress scales simplify to

$$\text{for large } \frac{F}{\sigma_0 d_c}, \quad [\sigma] \approx \sqrt{2f\rho gF}\tag{26}$$

$$[U] \approx \sqrt{\frac{2F}{f\rho g}}\,\frac{F}{\mu_0\delta}.\tag{27}$$

To summarize, for a given friction coefficient and cohesion, the driving force determines the depth of the active fault and the shear-stress scale. Knowledge of the rheology then allows the calculation of scales for the strain rate and the velocity.

4.2 A scaling law for the slip rate on the fault

Using dimensionless variables, the governing equations and boundary conditions depend on six dimensionless numbers:

$$\frac{F}{\sigma_0 d_c}, \quad \frac{[d]}{d_c}, \quad \frac{\beta[d]}{T_0}, \quad \frac{E}{RT_0}, \quad \frac{L_y}{[d]} \quad \text{and} \quad \frac{L_z}{[d]}.\tag{28}$$

We now show that this large set can be reduced to only one significant number. The first two numbers, $F/\sigma_0 d_c$, $[d]/d_c$ provide a measure of the importance of cohesion in the stress balance. For large F or small cohesion, both numbers are large and the results can be taken in the limit of these two numbers being infinite with small differences. This is to say that cohesion plays a subordinate role in the behaviour of a deep fault. The last two dimensionless numbers depend on the dimensions of the computational domain, L_y and L_z. Both take large values and hence once again do not influence the results significantly. In other words, fault zone behaviour is entirely determined by the local stress-field and is not sensitive to the size of the deforming medium. Another illustration of this will be given below. We conclude that only two dimensionless numbers are truly important, $\beta[d]/T_0$ and E/RT_0. The first provides a measure of the temperature difference between the top and bottom of the fault, and the second is a rheological parameter. Together with the viscosity law, these two numbers yield a third one, the viscosity variation over the fault zone, $\mu_0/\mu([d])$.

One further simplification derives from the observation that fault zone behaviour is not affected by deformation in the lower part of the domain. We therefore argue that the key dimensionless parameter is the local vertical viscosity variation over the fault, $\mu_0/\mu([d])$, which is a function of the two important dimensionless numbers listed above. If this analysis is correct, all dimensionless variables in the problem must be functions of this dimensionless number alone. To verify this, in Fig. 17 we show the dimensionless slip rate, $U_s/[U]$, as a function of
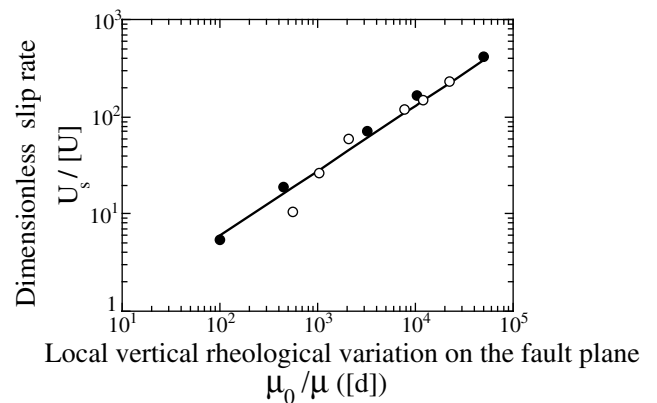
Figure 17. Dimensionless slip velocity $U_s/[U]$ as a function of vertical viscosity variation over the fault depth, $\mu_0/\mu([d])$. Black dots: calculations for fixed rheological stratification and variable fault depth. White dots: calculations for variable rheological stratification and fixed fault depth. The full straight line has a slope of 2/3, corresponding to a power-law relationship between the two variables.

$\mu_0/\mu([d])$. Indeed, taken together, all our results define a single relationship with little scatter and a plot close to a power law with a 2/3 exponent. The values for model 5 (Table 2), which has a different constitutive friction law for the fault, also fall on this relationship. The key controlling parameter is therefore the local viscosity variation over the fault.

The dimensionless slip rate $U_s/[U]$ provides a measure of strain localization on the fault and, conversely, can be used to assess the importance of distributed strain away from the fault. Thus, the scaling law of Fig. 17 simply states that, with increasing vertical viscosity variation, slip on the fault accounts for an increasing fraction of the total deformation. This law is valid for a range of activation energies implying a range of vertical variations of viscosity, as measured by the depth-scale δ in eq. (17). It is also unaffected by changes of friction law. Thus, we expect that it is not sensitive to the detailed form of the constitutive equations used in the model. Perhaps the most important point is that it does not involve the frictional strength, the magnitude of which remains highly controversial. In practice, one may measure directly most of the variables in the scaling law (fault depth, slip rate, far-field strain rate). This feature will be used below.

As expected, the dimensionless fault depth, $d/[d]$, is always close to 1, and tends to 1 as the vertical viscosity variation increases. For example, for $\mu_0/\mu([d]) = 5 \times 10^4$, one has $d/[d] = 0.94$. The limit of very large vertical viscosity variation is of course the relevant one for geological applications. In this limit, the depth-scale $[d]$ provides a very good estimate of the depth of an active fault. This shows that, for given far-field forcing, a weak fault (with a low friction coefficient) extends to larger depths than a strong fault (with high friction coefficient). This simple result had already been noted by several authors (e.g. Chery *et al.* 2001), but the scaling analysis goes further and shows how a change of frictional strength affects the slip rate on the fault through its effect on fault depth.

5 GEOLOGICAL IMPLICATIONS

The results obtained in this paper rely on several assumptions and hence must be used with caution to assess any specific shear zone. Strain localization below the fault should be enhanced with a non-linear strain-softening rheology. A single rheological equation was taken for the whole lithosphere. In reality, one should account for at least crust and mantle layers, but this would not affect the fault zone behaviour because it is not sensitive to the rheology of deep layers. Finally, the temperature field was taken as being horizontally uniform. Rheological laws for crustal rocks are strongly temperature dependent. Shear heating acts to increase temperatures in the vicinity of the fault, and hence the bulk effect is to increase the local vertical rheological variation and to localize the deformation further. However, this effect depends critically on the poorly-constrained frictional strength of faults. This uncertainty does not affect our scaling law for the slip rate (Fig. 17).

5.1 The far-field shear stress distribution

The vertical shear stress profile far from the fault zone is

$$\sigma_{yx}(L_y, z) = G\mu(z) = F \frac{\mu(z)}{\int_0^{L_z} \mu(z)\, dz} . \qquad (29)$$

This follows the vertical viscosity profile, as in classical calculations of lithosphere strength (Goetze & Evans 1979; Brace & Kohlstedt 1980). When interpreting this result, several factors must be borne in mind. One is that the top of the domain (at $z = 0$) does not correspond to the Earth's surface, but lies below an unconsolidated layer about 3 km thick where stresses conform to Byerlee's rule (Scholz 1998; Fig. 1). A second factor is that absolute values of stress depend on the magnitude of driving force F, which depends on the frictional strength of the fault (eq. 20). Finally, these results only hold for strike-slip deformation and have no validity for other tectonic regimes.

The maximum shear stress is achieved at the upper boundary:

$$\sigma_{yx}(L_y, 0) = F \frac{\mu_0}{\int_0^{L_z} \mu(z)\, dz} = \frac{F}{\delta} , \qquad (30)$$

where the rheological depth-scale δ is defined by eq. (17). The maximum shear stress increases with increasing vertical rheological variation and increasing driving force F. In an active region, one may determine the active fault depth d and derive estimates for F as a function of the frictional strength. In Figs 7 and 15, shear stress values have been scaled to the maximum stress on the fault, σ_d, and obviously exceeds the frictional strength of the fault near the upper boundary. Thus, other faults in the area can remain idle only if they are strong enough, i.e. with large enough friction coefficients, which corresponds to the 'weak fault in a strong crust' scenario (Zoback 2000). Faults with the same frictional properties would be set in motion and should be added to the model. However, this is not likely to change the ductile stress field significantly. As shown by Fig. 15, this stress field varies markedly over a horizontal distance approximately equal to d and settles to the far-field distribution at larger distances. Thus, for the near-fault stress field to be modified significantly, active faults must be distant by less than $2d$ from one another, which is seldom achieved in practice.

The relatively large stresses predicted by the model are achieved over a small vertical extent that is typically less than 2 km. For the Earth, adding the unconsolidated uppermost crustal layer, this corresponds to a depth interval of between about 3 and 5 km. At such shallow depths, the confining pressure may be small enough for the fracture strength to be larger than the frictional strength (Kohlstedt *et al.* 1995). In this case, only existing faults may be set in motion. If the fracture strength is exceeded, however, new faults must be generated implying that the mechanical model is not appropriate. Such a phenomenon requires a time-dependent calculation in which fault spacing is determined in a self-consistent manner, as in Roy & Royden (2000).

5.2 Distributed deformation away from strike-slip faults

We have derived a simple scaling law that states how the various variables depend on one another (Fig. 17). This result holds for a range of activation energies and characteristic depth-scale for rheological variations, and is expected to remain valid for other rheological laws. This scaling law may be rewritten as follows:

$$G = C \frac{U_s}{[d]} , \qquad (31)$$

where C is a constant of proportionality that depends on the vertical rheological variation over the fault. This rheological variation depends on the local geothermal gradient and on the activation energy for ductile flow, and is likely to be larger than 10^4 in most cases, especially in active zones with elevated geothermal gradients. Thus, from Fig. 17, the constant C is expected to be smaller than 10^{-2}. In practice, both the fault depth and the secular slip rate are known from seismic and deformation studies. Furthermore, with high-precision geodetic measurements, far-field strain rates may be determined, which allows an estimate of the constant C, which in turn yields constraints on crustal rheology and temperatures.

The key advantage of the scaling law is that there is no need to know the frictional properties of the fault, which only affect the absolute stress values. Thus, eq. (31) can be used to estimate the far-field strain rate regardless of how strong the fault really is. As an illustrative calculation, we use typical values for the San Andreas system: $U_s = 3$ cm yr^{-1} and $[d] = 10$ km. For $C \leq 10^{-2}$, we find that $G \leq 10^{-15}$ s^{-1}. This upper bound is precisely the strain rate value that is commonly adopted for estimates of lithosphere strength (Kohlstedt *et al.* 1995). More importantly, this is also the threshold value below which distributed deformation can be considered negligible for tectonic studies. This demonstrates that the properties of the continental upper crust do indeed lead to rigid-body motion away from strike-slip faults. From a more general perspective, the condition for rigid behaviour is that faulting extends to sufficiently large depths so that the local vertical rheological variation is large enough (Fig. 17). This may be achieved by small friction coefficients or locally enhanced temperature gradients.

5.3 Shear heating

The mechanical work done locally near an active fault includes both frictional and viscous components. The frictional component is given by

$$\phi_f = \sigma_{yx}(0, z) U_s(z),$$ (32)

with $0 \leq z \leq d$. Dimensional analysis gives a frictional heat scale:

$$[\phi_f] = \frac{[\sigma]^2 [d]}{\mu_0}.$$ (33)

The total amount of frictional heat is

$$W_f = \int_0^d \phi_f \, dz.$$ (34)

Ductile shear heating is given by two terms, corresponding to shear along vertical planes (φ_{yx}) and horizontal planes (φ_{zx}):

$$\varphi_d = \varphi_{yx} + \varphi_{zx} = \varphi_V + \varphi_H,$$ (35)

with $\varphi_{yx} = \sigma_{yx} \partial v_x / \partial y$ and $\varphi_{zx} = \sigma_{zx} \partial v_x / \partial z$. The viscous heat scale is given by

$$[\varphi_d] = \frac{[\sigma]^2}{\mu_0}.$$ (36)

The various components of shear heating for model 3 are shown in Figs 18 and 19. Ductile shear heating rates along horizontal and vertical planes have the same order of magnitude (Fig. 19).
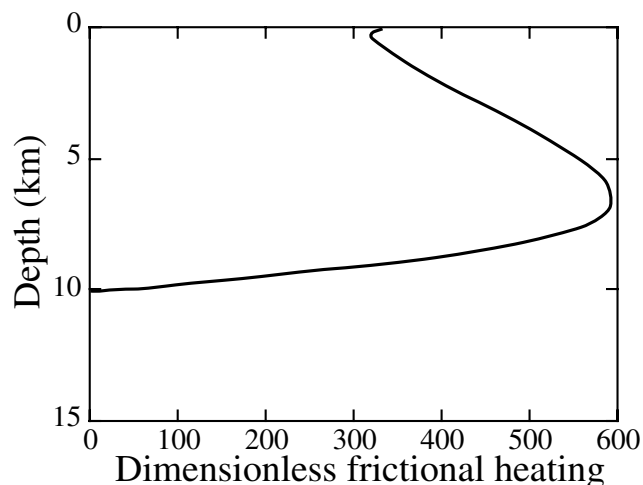

Figure 18. Dimensionless frictional shear heating for model 3, for which the base of the fault lies at 10 km depth.

Both are largest slightly above the base of the fault, which is also true for frictional shear heating (Fig. 18). Thus, temperature changes owing to shear heating will be most dramatic above the base of the fault, with important consequences for rheology and for strain localization.

The total amount of heat generated by viscous dissipation is

$$W_d = \int\!\!\int \varphi_d \, dy \, dz = W_V + W_H.$$ (37)

This integral includes a large contribution caused by the large stresses and strain rates in the vicinity of the fault, and a much smaller contribution involving stresses at large horizontal distances away from the fault. This second contribution is an increasing function of the width of the computational domain, L_y, and hence is not relevant to a local analysis. We therefore consider only the first contribution, which we estimate
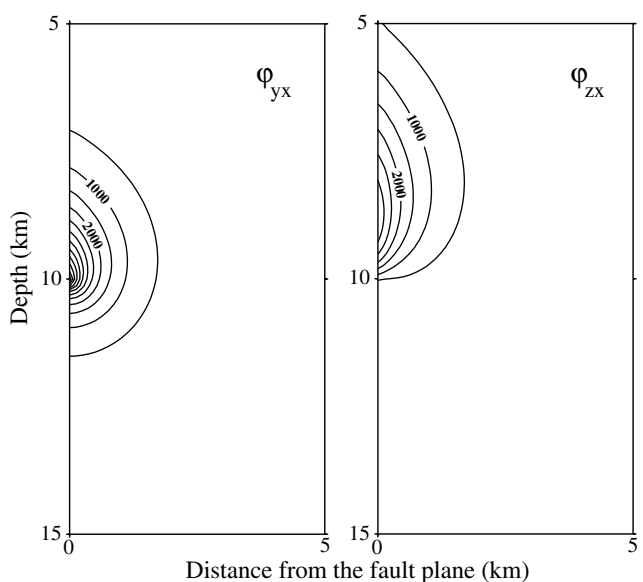

Figure 19. Dimensionless viscous shear heating for model 3 (Table 2), for which the base of the fault lies at 10 km depth. φ_{yx} and φ_{zx} are the contributions from shear on vertical and horizontal planes, respectively.

Table 5. Mechanical work arising from friction on the fault (W_f) and viscous dissipation arising from ductile deformation (W_d). W_V denotes dissipation caused by shear stresses on vertical planes parallel to the fault.

$\mu_0/\mu([d])$	W_f/W_d*	W_V/W_d*
10^2	0.64	0.76
5.6×10^2	1.12	0.61
3.2×10^3	1.78	0.52
7.9×10^3	2.06	0.52 †
2.3×10^4	2.33	0.51

*: dimensionless
†: model 3

over a fixed (and arbitrary) horizontal distance of 15 km. Changing this distance by a few kilometres does not affect the quantitative result in any significant manner. The respective importance of frictional and ductile shear heating varies depending on the vertical rheological variation over the fault. For fixed far-field force F (Table 5), increasing the rheological variation over the fault plane acts to increasingly localize deformation in the vicinity of the fault. Consequently, frictional heating becomes increasingly important (Fig. 20).

The scales for the frictional and ductile components of shear heating, W_f and W_d, are identical and equal to $[\sigma]^2[d]^2/\mu_0$. Substituting for the stress and depth scales, in the limit of no cohesion, one finds that this scale does not depend on f, the friction coefficient. Thus, the total amount of heat generated does not depend on f, which reflects the global energy balance in the system. For a given force F, changing the friction coefficient acts to change shear stresses on the fault, but it also acts to change the fault depth, and hence the size of the region over which heat is dissipated. For example, decreasing the friction coefficient acts to deepen the fault and to generate heat over a larger volume, implying a smaller temperature rise.

With shear heating, the local thermal structure at the vicinity of the fault differs from the regional structure and may vary with time. It is premature to speculate how shear heating affects fault behaviour, however, it obviously acts to increase the local rheological variation over the fault and hence is likely to enhance slip over ductile deformation near the surface.
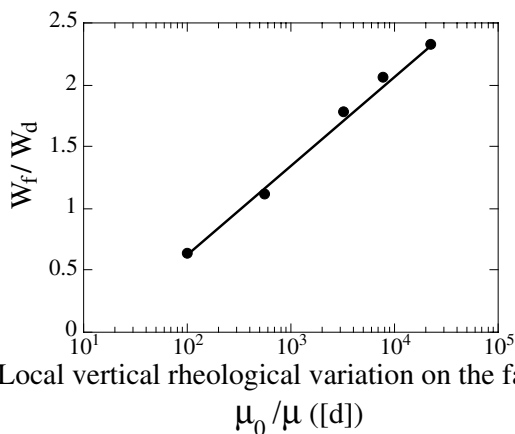

Local vertical rheological variation on the fault plane
μ_0/μ ([d])

Figure 20. Ratio between frictional and viscous shear heating as a function of vertical viscosity variation over the fault depth.

5.4 Vertical variations of the slip rate on a fault

The vertical distribution of seismic slip on a fault, together with the length of the fault zone which is set in motion during an earthquake, determines the short-term stress field following an earthquake. The present model predicts that distributed deformation extends over a large fraction of the fault depth (Fig. 9). This result pertains to the secular slip rate on the fault, and hence should be compared with the cumulative slip over a whole seismic cycle. Unfortunately, such data are not available yet, but it does seem that, save for creeping fault segments, coseismic displacements contribute the largest part of the slip budget of a fault. Precise measurements of coseismic and post-seismic displacements are available for two recent earthquakes, at Landers, California, in 1992 (Hernandez *et al.* 1999; Pollitz *et al.* 2000) and Izmit, Turkey, in 1999 (Reilinger *et al.* 2000). Post-seismic displacements are caused by viscous relaxation in the lower crust and only account for 10 per cent of the coseismic displacements (Pollitz *et al.* 2000; Reilinger *et al.* 2000). At Landers, the interseismic velocity field over 3.5 years is dwarfed by the post-seismic velocity field (Pollitz *et al.* 2000). On both faults, therefore, coseismic slip values probably allow reasonable estimates for the vertical profile of secular slip rate. These data demonstrate that, on average, slip is largest at the surface and progressively decreases with depth (Hernandez *et al.* 1999; Reilinger *et al.* 2000), much in the manner illustrated in Fig. 9.

5.5 Discussion

The present model emphasizes that, in regions with major faults, stresses vary horizontally over small distances at relatively shallow depths in the crust. Another point is that the secular slip rate on the fault progressively decreases to zero in a thick transition zone where deformation also involves ductile flow. Previous models rely on simplified representations of the coupling between brittle and ductile regions. For example, brittle behaviour is usually confined to an upper layer of constant thickness in which velocities and slip rates do not vary with depth (e.g. Thatcher & England 1998; Leloup *et al.* 1999). That this really happens in nature cannot be demonstrated by available data, and hence represents a strong assumption on fault behaviour. This assumption affects the distributions of stress and strain rate in the ductile region, as well as the magnitude of shear heating. One consequence is that shear heating is largest at the base of the fault, contrary to our results (Figs 18 and 19). Another consequence is that the horizontal component of ductile shear heating, W_H, is much smaller than the vertical component, W_V (Leloup *et al.* 1999), whereas both have similar magnitudes in our model (Table 5).

6 CONCLUSION

The simple mechanical model of this study emphasizes that it is not possible to impose independently the far-field driving velocity or force, the depth of a fault and the vertical profile of slip rate on the fault. For a given friction law, the driving force imposes the depth of the fault that becomes activated. For weak vertical rheological variations and shallow faults, near-surface deformation is distributed over a wide region and only a small fraction is accommodated by sliding on the fault. For large vertical rheological variations and deep faults, most of the

deformation is accommodated by sliding on the fault. To localize deformation, large rheological variations or deeply rooted faults are required. These two characteristics are equivalent and a single parameter is sufficient to describe fault behaviour: the vertical rheological variation over the depth of the fault. A scaling law independent of fault strength relates the slip rate and the far-field strain rate.

Owing to the complex stress distribution in the vicinity of the fault zone, strain localization may occur at depth without local strain or thermal softening. In geological conditions, such that vertical rheological variations are large, quasi-rigid behaviour is predicted for the near-surface environment. However, at depth, the slip rate varies significantly over a large fraction of the fault vertical extent in a large adjustment zone with both slip and ductile deformation.

ACKNOWLEDGMENTS

REFERENCES

Bourne, S.J., England, P.C. & Parsons, B., 1998. The motion of crustal blocks driven by flow of the lower lithosphere and implications for slip rates of continental strike-slip faults, *Nature,* **391,** 655–659.

Byerlee, J.D., 1978. Friction of rocks, *Pure appl. Geophys.,* **116,** 615–625.

Brace, W.F. & Kohlstedt, D.L., 1980. Limits on lithospheric stress imposed by laboratory experiments, *J. geophys. Res.,* **85,** 6248–6252.

Carter, N.L. & Tsenn, M.C., 1987. Flow properties of continental lithosphere, *Tectonophysics* **136,** 27–63.

Chery, J., Zoback, M.D. & Hassani, R., 2001. A simplified 3-D thermomechanical model of the San Andreas fault in central and northern California, *J. geophys. Res.,* in press.

Goetze, C. & Evans, B., 1979. Stress and temperature in the bending lithosphere as constrained by experimental rock mechanics, *Geophys. J. R. astr. Soc.,* **59,** 463–478.

Hernandez, B., Cotton, F. & Campillo, M., 1999. Contribution of radar interferometry to a two-step inversion of the kinematic process of the 1992 Landers earthquake, *J. geophys. Res.,* **104,** 13 083–13 100.

King, G.C.P., Stein, R. & Rundle, J.B., 1988. The growth of geological structures by repeated earthquakes, 1. Conceptual framework, *J. geophys. Res.,* **93,** 13 307–13 318.

Kohlstedt, D.L., Evans, B. & Mackwell, S.J., 1995. Strength of the lithosphere: constraints imposed by laboratory experiments, *J. geophys. Res.,* **100,** 17 587–17 602.

Kirby, S.H. & Kronenberg, A.K., 1987. Rheology of the lithosphere: selected topics, *Rev. Geophys.,* **89,** 1219–1244.

Lachenbruch, A. & Sass, J.H., 1980. Heat flow and energetics of the San Andreas fault zone, *J. geophys. Res.,* **85,** 6185–6222.

Lachenbruch, A.H. & Sass, J.H., 1992. Heat flow from Cajon Pass, *J. geophys. Res.,* **97,** 4995–5015.

Leloup, P.H., Ricard, Y., Battaglia, J. & Lacassin, R., 1999. Shear heating in continental strike-slip shear zones: model and field examples, *Geophys. J. Int.,* **136,** 19–40.

Mori, J. & Abercrombie, R.E., 1997. Depth dependence of earthquake frequency–magnitude distributions in California: implications for rupture initiation, *J. geophys. Res.,* **102,** 15 081–15 090.

Pollitz, F.F., Peltzer, G. & Bürgmann, R., 2000. Mobility of continental mantle: evidence from postseismic geodetic observations following the 1992 Landers earthquake, *J. geophys. Res.,* **105,** 8035–8054.

Reilinger, R.E., Ergintav, S., Bürgmann, R., McClusky, S., Lenk, O., Barka, A., Gurkan, O., Hearn, L., Feigl, K.L., Cakmak, R., Aktug, B., Ozener, H. & Töksoz, M.N., 2000. Coseismic and postseismic fault slip for the 17 August 1999, $M = 7.5$, Izmit, Turkey earthquake, *Science,* **289,** 1519–1524.

Ricard, Y., Froidevaux, C. & Hermance, J.F., 1983. Model heat flow and magnetotellurics for the San Andreas and oceanic transform faults, *Annales Geophysicae,* **1,** 47–52.

Roy, M. & Royden, L.H., 2000. Crustal rheology and faulting at strike-slip plate boundaries, 2, Effects of lower crustal flow, *J. geophys. Res.,* **105,** 5599–5613.

Savage, J.C., 1990. Equivalent strike-slip earthquake cycles in half-space and lithosphere–asthenosphere Earth models, *J. geophys. Res.,* **95,** 4873–4879.

Savage, J.C., Svarc, J.L. & Prescott, W.H., 1999. Geodetic estimates of fault slip rates in the San Francisco Bay area, *J. geophys. Res.,* **104,** 4995–5002.

Schaff, D.P., Bokelmann, G.H.R., Beroza, G.C., Waldhauser, F. & Ellsworth, W.L., 2001. High resolution image of Calaveras fault seismicity, *J. geophys. Res.,* in press.

Scholz, C.H., 1980. Shear heating and the state of stress on faults, *J. geophys. Res.,* **85,** 6174–6184.

Scholz, C.H., 1990. *The Mechanics of Earthquakes and Faulting,* pp. 439, Cambridge University Press, Cambridge.

Scholz, C.H., 1998. Earthquakes and friction laws, *Nature,* **391,** 37–42.

Scholz, C.H., 2000. Evidence for a strong San Andreas fault, *Geology,* **28,** 163–166.

Sibson, R.H., 1986. Earthquakes and rock deformation in crustal fault zone, *Ann. Rev. Earth planet Sci.,* **14,** 149–175.

Sleep, N.H. & Blanpied, M.L., 1992. Creep, compaction and the weak rheology of major faults, *Nature,* **359,** 687–692.

Thatcher, W., Present-day crustal movements and the mechanics of cyclic deformation, The San Andreas fault system, California, *US Geological Survey Professional Paper,* **1515,** 189–205.

Thatcher, W. & England, P.C., 1998. Ductile shear zones beneath strike-slip faults: implication for the thermomechanics of the San Andreas fault zone, *J. geophys. Res.,* **103,** 891–905.

Townend, J. & Zoback, M.D., 2000. How faulting keeps the crust strong, *Geology,* **28,** 399–402.

Turcotte, D.L., Tag, P.H. & Cooper, R.F., 1980. A steady state model for the distribution of stress and temperature on the San Andreas fault, *J. geophys. Res.,* **85,** 6224–6230.

Yuen, D.A., Fleitout, L., Schubert, G. & Froidevaux, C., 1978. Shear deformation zones along major transform faults, *Geophys. J. R. astr. Soc.,* **54,** 93–119.

Zoback, M.D., 2000. Strength of the San Andreas, *Nature,* **405,** 31–32.